Multifractal Analysis of Snowfall Recorded Using a 2D Video Disdrometer

Timothy H. Raupach, Auguste Gires, Ioulia Tchiguirinskaia, D Schertzer, Alexis Berne

Multifractal Analysis of Snowfall Recorded Using a 2D Video Disdrometer

TIMOTHY H. RAUPACH

Environmental Remote Sensing Laboratory, École Polytechnique Fédérale de Lausanne, Lausanne, Switzerland

AUGUSTE GIRES, IOULIA TCHIGUIRINSKAIA, AND DANIEL SCHERTZER

Hydrology Meteorology and Complexity, École des Ponts, UPE, Champs-sur-Marne, France

ALEXIS BERNE

Environmental Remote Sensing Laboratory, École Polytechnique Fédérale de Lausanne, Lausanne, Switzerland

(Manuscript received 9 September 2016, in final form 13 April 2017)

ABSTRACT

Universal multifractal (UM) analysis was used to investigate the scaling properties of snowfall at high temporal and spatial resolutions. Snowfall data were recorded using a 2D video disdrometer (2DVD) in the Swiss Alps. Six 1-h-long periods of snowfall, half in calm and half in light wind conditions, were selected for analysis. UM analysis was performed on reconstructed 35-m vertical columns of snowfall structure, snowfall time series at 100-ms resolution, and two-dimensional snowflake accumulation maps over a $5.12 \times 5.12\ \text{cm}^2$ area. Multifractal scaling was observed for the vertical structure of snow particle number concentration, for scales between about 35 and 4.4 m, and sometimes down to about 0.5 m. At smaller scales, no scaling was observed. In high-resolution time series of snowfall, evidence of scaling was found for scales between about 7 min and ~26 s in most of the analyzed hours. Snowflake accumulations within a subset of the small sampling area of the 2DVD showed no scaling properties, suggesting homogeneous structure in snowfall at the very small (~5 cm) scale, which agrees with the results for vertical structure and time series.

1. Introduction

Multifractal analysis is a useful way to study the properties of precipitation fields. It can provide insights into their intermittency and extremes and whether they are invariant to scale or exhibit one or more scaling regimes in time or space. The framework of universal multifractals (UMs; Schertzer and Lovejoy 1987a, 1997) has been used to analyze rainfall over a wide variety of scales (see, e.g., reviews by Lovejoy and Schertzer 1995; Schertzer et al. 2010). Few studies have examined the multifractal properties of snowfall. In this paper we report on multifractal analyses of snowfall recorded using a 2D video disdrometer (2DVD; Kruger and Krajewski 2002; Schönhuber et al. 2008) situated in the Swiss Alps.

A wide variety of data sources have been used to study the multifractal properties of precipitation. At the large and medium scales, coarser than a few kilometers in space or a few minutes in time, satellite products (Tessier et al. 1993; Lovejoy et al. 2008), climate simulations (Royer et al. 2008), weather model outputs (Gires et al. 2011), weather radars (Nykanen and Harris 2003; Verrier et al. 2010; Gires et al. 2011), and rain gauge data (e.g., Fraedrich and Larnder 1993; Olsson 1995; Tessier et al. 1996; De Lima and Grasman 1999; Molnar and Burlando 2008; De Lima and De Lima 2009) have been used. At smaller scales, studies have used lidar (Mandapaka et al. 2009) and disdrometer measurements (De Montera et al. 2009; Gires et al. 2014, 2016).

Previous multifractal work has mostly focused on liquid precipitation. Molnar and Burlando (2008) studied gauged precipitation in Switzerland and found stronger multifractality in summer precipitation than winter precipitation, which was close to monofractal. They posited that intraseason variability in scaling parameters could be caused by mixed rain and snow at some locations and recommended a study of snow-only scaling parameters. Shook and Pomeroy (2010) studied time series of daily snowfall on the Canadian Prairies and found weak multifractality for scales shorter than 1 month. Spatial distributions of snow accumulations have been shown to demonstrate fractal behavior

Corresponding author: Timothy H. Raupach, timothy.h.raupach@gmail.com

DOI: 10.1175/JHM-D-16-0224.1

(e.g., Shook and Gray 1996, 1997; Granger et al. 2002; Iggy Litaor et al. 2002; Deems et al. 2006). Fabry (1996) used spectral analysis to study high-resolution time series (down to 0.1 s) of precipitation, including snow, captured using a sonic gauge. They performed spectral analysis and observed scaling in the snowfall time series with a break at about 20 s, after which little scaling was observed. They attributed the difference in scaling regimes to mixing-like processes caused by the differing fall speeds of the hydrometeors.

In this study we used similar methodology to analyses that were previously made on liquid precipitation by Gires et al. (2015), applied to measurements of solid precipitation. Gires et al. (2015) used data collected using a 2DVD to analyze raindrop distributions at high resolution in space and time. During the heaviest portions of their studied rainfall events, they found scaling behavior in vertical rainfall structure at ranges from 0.5 to 36 m, and homogeneously distributed raindrops at smaller scales. In this study we used the same instrument and performed the same analyses on data recorded in the Swiss Alps in winter, to test whether multifractality is evident in snowfall at high spatial and temporal resolutions. This study is a first application of multifractal analysis to snow data for horizontal accumulations of individual snowflakes and reconstructed vertical columns of snowflake concentration and mass, and to the best of our knowledge this is the first time that full UM analysis has been used on snowfall-only data at temporal resolutions finer than 1 day. The existence of scaling behavior in snowfall at typical instrument sampling area scales could have implications for the measurement of snowfall at point locations, which is subject to large uncertainties (e.g., Yang 2014). In this study we test whether snowfall exhibits scaling behavior at such small scales, using high-resolution data.

The rest of this paper is organized as follows. A brief review of UM analysis is given in section 2. The data used are presented in section 3. In section 4 the methods used to treat the data are shown. Results are shown in section 5, and conclusions are drawn in section 6.

2. UM analysis

In this section, we briefly explain multifractal analysis with the aim of showing the meaning behind the variables we analyze in the following sections. For more detail, the reader is encouraged to refer to the review of Schertzer and Lovejoy (2011) and references therein. Let ε_λ be a field at resolution λ. This field has a spatial dimension d. An example of a one-dimensional field is a time series of rain rate measurements, and an example of a two-dimensional field is the positions of snowflakes on a plane. The resolution of the field is $\lambda = L/l$, where L is the outer scale—the length of the time series, or the side length of the plane—and l is the observation scale. The field contains a process that is assumed to have a mean of one over its outer scale. In this work, data are normalized by dividing all measured values by the overall ensemble mean.

Let A be the set of points where the process is active. In a fractal process, the number of nonoverlapping d-dimensional boxes with side length l required to cover all the process points in the field $N_{\lambda,A}$ is related to the resolution (e.g., Lovejoy et al. 1987) via the fractal dimension D_F:

$$N_{\lambda,A} \approx \lambda^{D_F}. \tag{1}$$

A sparse set will be covered by fewer boxes, so the fractal dimension is a measure of sparseness of the process within its outer scale. Given any single one of these boxes, the probability that it intersects with the process set A is

$$\Pr(\varepsilon_\lambda) = \frac{N_{\lambda,A}}{N_\lambda} \approx \frac{\lambda^{D_F}}{\lambda^d} = \lambda^{-c_F}, \tag{2}$$

where N_λ is the number of boxes required to cover the entire field, and $c_F = d - D_F$ is called the fractal codimension of the process.

The sparseness of the process and the fractal dimension will change if the process is thresholded by a value (e.g., Lovejoy et al. 1987). To characterize not just the process occurrence but also its values, then, a scale-dependent threshold λ^γ can be used. The probability that a single box intercepts the thresholded field is then

$$\Pr(\varepsilon_\lambda \geq \lambda^\gamma) \approx \lambda^{-c(\gamma)}, \tag{3}$$

where γ is a called a singularity and $c(\gamma)$ is called the fractal codimension function (Schertzer and Lovejoy 1987a).

It can be shown (Schertzer and Lovejoy 1987a) that Eq. (3) is equivalent to a relationship between the statistical moments of the field and its resolution, such that

$$\langle \varepsilon_\lambda^q \rangle \approx \lambda^{K(q)}, \tag{4}$$

where $\langle \varepsilon_\lambda^q \rangle$ is the (ensemble) mean of ε_λ^q, q is a moment order, and $K(q)$ is called the moment scaling function. Function $K(q)$ is related to $c(\gamma)$ via the Legendre transform (Parisi and Frish 1985), and for any moment q there is an associated singularity γ. Knowledge of $K(q)$ thus allows for the field to be characterized at any resolution. In the UM framework, $K(q)$ can be written as an expression depending on only three parameters (Schertzer and Lovejoy 1987a, 1997):

$$K(q) = \frac{C_1}{\alpha - 1}(q^\alpha - q) - Hq. \quad (5)$$

The parameters are as follows:

1) The degree of nonconservation H measures the scale-dependence of the mean (of the field), such that $\langle \varepsilon_\lambda \rangle \approx \lambda^{-H}$. Parameter $H = 0$ for a conservative field in which $\langle \varepsilon_\lambda \rangle = 1$ at all resolutions, and H is also the order of fractional integration (if H is negative) or derivation (if H is positive) required to transform the observed field into a conservative field (Schertzer and Lovejoy 1991; Tessier et al. 1993).
2) The mean intermittency C_1 is the fractal codimension of the mean field. The mean field is the field thresholded by the singularity associated with $q = 1$. This singularity is also equal to C_1 if the field is conservative (Schertzer and Lovejoy 2011). If $C_1 = 0$ then the mean field is homogeneous. A larger C_1 indicates a sparser mean field. For nonnull fields, $0 \le C_1 \le d$.
3) The multifractality index α indicates how quickly the intermittency of the field changes as the considered singularity moves away from that associated with $q = 1$, the singularity of the mean field. It thus measures where the process sits on a scale between monofractality (for which $\alpha = 0$ and the intermittency is the same for all thresholds) and log normality ($\alpha = 2$).

Spectral analysis is used to find H and provides a first estimate of the scaling behavior of the field. If the field is multifractal then its power spectra E can be written

$$E(k) \approx k^{-\beta}, \quad (6)$$

where k is the wavenumber and β is called the spectral slope, and parameter H is then estimated as (Tessier et al. 1993)

$$\beta = 1 + 2H - K(2), \quad (7)$$

with H taken as zero in Eq. (5) (i.e., considering only the conservative part). For a given value of q, trace moment (TM) analysis (e.g., Schertzer and Lovejoy 1987b) can be used to find $K(q)$: on a log–log plot of λ on the x axis versus $\langle \varepsilon_\lambda^q \rangle$ on the y axis, the slope of the line of best fit is $K(q)$.

The values of C_1 and α for a given field can be found directly using double trace moment (DTM) analysis (Lavallée et al. 1993), in which the η power of the field is used. The η power is written $\varepsilon_\lambda^{(\eta)}$ and is calculated by raising the field to the ηth power at maximum resolution, then upscaling. The qth statistical moment of the η-power field also scales with resolution as described by a moment scaling function $K(q, \eta)$, such that

$$\langle \varepsilon_\lambda^{(\eta)q} \rangle \approx \lambda^{K(q,\eta)}, \quad (8)$$

and in the case of the UM framework,

$$K(q, \eta) = \eta^\alpha K(q). \quad (9)$$

DTM analysis uses a log–log plot of η on the x axis versus $K(q, \eta)$ on the y axis; on the linear part of the plot, the slope is equal to α and the intercept provides C_1 (Lavallée et al. 1993).

TM and DTM analyses rely on the assumption that the field is conservative. When $H \neq 0$, the field is considered nonconservative and an additional fractional integration is required before TM and DTM analyses are used to estimate α and C_1 (Schertzer and Lovejoy 1991; Tessier et al. 1993; De Montera et al. 2009). In this work we used a fractional integration in which each one-dimensional realization was transformed individually (see Schertzer and Lovejoy 1991, appendix B2). When required, these transformations were performed after the fields had been divided by the ensemble mean. For a one-dimensional field ε, let $I = \varepsilon - \langle \varepsilon \rangle$, and let $\mathcal{F}(I)$ be the Fourier transform of I, i be the complex unit, and k be the wavenumber. The fractionally integrated field $\hat{\varepsilon}$ was calculated as

$$\mathcal{F}(\tilde{\varepsilon}) = ik^H \mathcal{F}(I), \quad (10)$$

$$\hat{\varepsilon} = \frac{\tilde{\varepsilon} - \min(\tilde{\varepsilon})}{\langle \tilde{\varepsilon} - \min(\tilde{\varepsilon}) \rangle} \langle \varepsilon \rangle. \quad (11)$$

Note that an inverse Fourier transform is used to convert $\mathcal{F}(\tilde{\varepsilon})$ to $\tilde{\varepsilon}$, and that as well as subtracting the mean of ε, the zeroth Fourier component was set to zero to force the mean of each field to be zero (e.g., Tessier et al. 1993). This fractional transformation corresponds to integration when $H < 0$ and derivation when $H > 0$.

Finite sample sizes mean that there is a maximum singularity γ_s for which reliable estimates of the codimension and moment scaling functions are possible (e.g., Hubert et al. 1993). Parameter γ_s has an associated maximum moment-order q_s. To calculate the field at a given resolution, the measured data (at high resolution) are upscaled through an iterative process, in which at each step the observation scale l is doubled to create a lower-resolution field by averaging adjacent pixels. For this reason, the outer scale of the field must be a power of two.

3. Data

The data used in this study were collected using a 2DVD (of low-profile type) located at Weissfluhjoch Versuchsfeld (46.8301°N, 9.8096°E) near Davos, Switzerland. The site is in an alpine environment 2540 m above mean sea level. The 2DVD was placed on a

FIG. 1. (left) The DFIR structure and (right) the 2DVD instrument installed on a platform between the two fences near Davos, Switzerland.

platform about 2 m above the ground, between the two fences of a double fence intercomparison reference (DFIR; e.g., Goodison et al. 1998) structure. Data used in this study were collected during the northern winter of 2014/15. Figure 1 shows the installed instrument.

The 2DVD contains two perpendicularly facing line-scan cameras, each with an opposing light source, which detect the shadow, from two angles, of any particle that falls through its collection area. The imaging resolution is finer than 0.2 mm, and the nominal collection area is approximately $10 \times 10\,\text{cm}^2$ (Schönhuber et al. 2007). The two camera planes are vertically offset so that particle velocity is measured directly, through the difference in particle detection time in each camera. The relative orientation of the two planes is measured using a calibration procedure and set as a software parameter. The shape of each particle can be reconstructed using the two views (Schönhuber et al. 2008). The 2DVD cannot be considered an absolute reference for snow measurements (Battaglia et al. 2010), and for liquid precipitation it has been shown to underestimate raindrops under 0.3 mm in equivolume diameter (Tokay et al. 2013). This being said, it is able to provide data on individual snowflakes at high resolutions, so it remains useful for this study.

There were collocated meteorological instruments at the 2DVD location, and we used data from these instruments to select three 1-h periods during which there was snowfall and calm wind conditions (mean wind speed under $1.75\,\text{m s}^{-1}$), and three 1-h periods in which there was snowfall and light winds (mean wind speed greater than $1.75\,\text{m s}^{-1}$ and less than $5\,\text{m s}^{-1}$). Wind speed was measured outside the DFIR by two Young 05103 Wind Monitors at two heights (3.5 m at 1-min resolution and 5.5 m at 30-min resolution), temperature was measured outside the DFIR by a Thygan VTP 6 instrument, and precipitation was measured inside the DFIR by a Thies Laser Precipitation Monitor disdrometer [see Roulet et al. (2014) for information on the meteorological instruments]. We found, using the meteorological data, 1-h periods in which there was snowfall without rain or hail (as identified by the Thies instrument SYNOP code 4677) and a temperature of less than −3°C. These times were matched to hours during which the 2DVD recorded snowflakes with no reported errors or missing time periods. For each day considered, the matching hour with the most solid precipitation was selected. Of these selected hours, the three with maximum solid precipitation for calm winds and light winds, respectively, were analyzed. The resulting time periods (henceforth referred to by event number) are summarized in Table 1.

Particles measured by the 2DVD were processed using the 2DVD manufacturer's software and then filtered and "rematched" based on work by Hanesch (1999) and

TABLE 1. Information on the studied hours of precipitation by event number (E), showing the studied time, mean wind speed at 3.5 m [W3.5 ($m\,s^{-1}$)], mean wind speed at 5.5 m [W5.5 ($m\,s^{-1}$)], mean solid precipitation intensity measured by Thies laser disdrometer [Int ($mm\,h^{-1}$)], mean temperature [Temp (°C)], and the number of particles measured by the 2DVD during the hour (N). The first three selected hours are for calm winds, the second three for light winds.

E	End of hour	W3.5	W5.5	Int	Temp	N
1	1800 UTC 17 Dec 2014	0.7	0.9	1.3	−5.3	17 256
2	1100 UTC 26 Dec 2014	0.2	1.6	1.9	−12.3	11 878
3	0700 UTC 11 Jan 2015	1.6	0.4	2.7	−4.3	13 477
4	1300 UTC 28 Dec 2014	2.2	4.3	1.7	−13.2	11 453
5	0700 UTC 27 Jan 2015	4.7	4.2	3.0	−11.1	13 432
6	1400 UTC 8 Feb 2015	4.1	4.6	5.3	−15.1	17 232

Huang et al. (2010). For consistency with the manufacturer's filtering, the rematching was made with an output velocity range from 0.5 to 6 $m\,s^{-1}$, and particles wholly within the first 512 pixels of both camera lines (before rematching) were used. Particles that only covered one line were excluded. The results of this multifractal analysis appear robust to varying rematching assumptions. The 2DVD data contained, for each particle, the time stamp (to the millisecond), velocity ($m\,s^{-1}$), the particle width and height recorded by each camera (mm), and the pixel number of the center of the particle in lines from each camera. We selected data from the six 1-h periods, plus 10 min after each one. Particles that were recorded in the 10 min after each event were used only for reconstruction of the vertical column at the end of the events. During these periods, 109 961 valid particles were recorded. The measurement area of the 2DVD is not a rectangle (Schönhuber et al. 2008), and the width of each pixel in millimeters depends on its distance from the camera. We selected all particles wholly within a $88 \times 88\,mm^2$ region inside the measurement area and calculated the center positions in millimeters of each particle from the bottom-left point of this region. After this selection, 101 013 particles remained (~8% were not in the selected region). To ensure we sampled snowfall only, particles were only kept if their velocities were less than 3 $m\,s^{-1}$ [following the classification shown in Löffler-Mang and Joss (2000)]; this constraint removed 4.8% of the remaining particles.

4. Data treatment

In this section, the ways that the 2DVD snow particle data were treated before applying multifractal analysis are presented. The mass of each solid precipitation particle was estimated (section 4a). These masses were then formed into reconstructed ballistic columns (section 4b) and time series (section 4c). Two-dimensional particle accumulation maps (section 4d) were also calculated.

a. Estimation of particle masses

The method of Huang et al. (2015) was used to estimate the mass of each recorded particle from the 2DVD data. Their method is an inversion of the equations of Böhm (1989), applied to 2DVD data. Using this technique, the mass m (in grams) of a particle is calculated as

$$m = \frac{10^3 \pi \eta_{\rm air}^2 X}{8 g \rho_a} \left(\frac{A_e}{A_c}\right)^{1/4}, \tag{12}$$

where $\eta_{\rm air}$ ($kg\,m^{-1}\,s^{-1}$) is the air viscosity, ρ_a ($kg\,m^{-3}$) is the air density, and g ($m\,s^{-2}$) is acceleration due to gravity. Parameter A_e (m^2) is the projected "shadow" area of the particle, and A_c (m^2) is its smallest circumscribed area, both taken in a plane normal to the flow. For application to 2DVD data, A_e is taken as the area of pixels covered by the particle in one camera view, and A_c as the area of the minimum ellipse or circle that covers the particle in the same camera view. The assumption that the ratio of areas is independent of viewing angle was called "reasonable" by Szyrmer and Zawadzki (2010). We have added the multiplier of 10^3 to convert the mass to grams. Variable X (unitless) is the Davies number, calculated as

$$X = \left\{ \frac{\left[\left(\frac{\rm Re}{8.5}\right)^{(1/2)} + 1\right]^2 - 1}{0.1519} \right\}^2, \tag{13}$$

and Re (unitless) is the Reynold's number, which depends on the particle velocity V_f ($m\,s^{-1}$):

$$\mathrm{Re} = \frac{2 \rho_a V_f}{\eta_{\rm air}} \left(\frac{A_c}{\pi}\right)^{1/2}. \tag{14}$$

The viscosity and air density were calculated per event for the 2DVD site. Since viscosity is mainly affected by temperature, in this work we used the viscosity of dry air. Air density was calculated assuming a relative humidity of 85%. The average viscosity was $1.672 \times 10^{-5}\,kg\,m^{-1}\,s^{-1}$, and the average air density was $0.974\,kg\,m^{-3}$. Particle areas were calculated using data from one of the 2DVD's two cameras (camera A). For a given particle, A_e was calculated as the area of the ellipse with major and minor axes equal to the major and minor axes of the bounding rectangle of the particle. Following Huang et al. (2015), if A_e/A_c was greater than one, A_c was replaced by the area of the smallest circle containing the bounding rectangle. Densities of estimated mass are shown by event in Fig. 2.

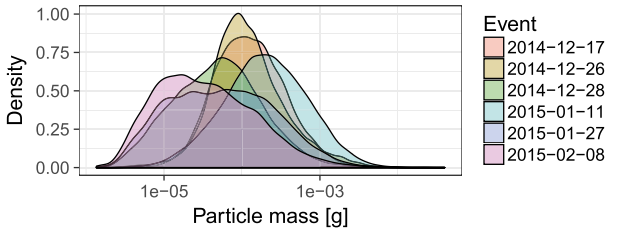

FIG. 2. Densities of estimated particle mass by event in chronological order. The x axis has a log scale.

b. *Reconstruction of vertical columns*

Just as in Gires et al. (2015), we reconstructed vertical columns above the 2DVD. Each reconstructed column had dimensions of $0.088 \times 0.088 \times 35\,\mathrm{m}^3$, and we reconstructed one column per second of the studied precipitation. For each second, the height above the instrument for every particle was calculated using the particle's velocity (as measured at the 2DVD), and its center point, and those within 35 m of the instrument were kept. Each column was divided vertically into 512 boxes, so that each box had a height of about 68 mm. This reconstruction of vertical columns relies on the assumptions that there was no wind, that particles fell vertically at constant velocity, and that there were no microphysical processes such as aggregation or breakup of snowflakes. The grouping of particles into vertical boxes goes some way toward reducing the effect of ignoring horizontal movement of the snowflakes and turbulence, but these remain very coarse assumptions. Our aim in this study is to gain some preliminary insights into the vertical structure of falling snow, in the absence of measurements of the true vertical snow column, so we continue in spite of these obvious limitations. We note that the other two spatiotemporal "cuts" we use—time series and particle accumulations—do not rely on these assumptions. Examples of two reconstructed columns are shown in Fig. 3.

The quantity analyzed was calculated per time and per box as

$$X_p = \sum_n^{N_P} m_n^p, \tag{15}$$

where the sum was taken over all N_P particles in the box. By varying p, different quantities are recovered; X_0 provides the number of particles per box, while X_1 equals the total estimated snow mass per box. We study fields for p equal to 0, 0.5, and 1, with 0.5 included to show the trend between the two end points. Each set of 512 values for 1 s of precipitation was assumed to represent one realization of the solid precipitation process in the vertical column, and multifractal analysis was performed on these realizations. As a control dataset, we also randomly redistributed the particle center points

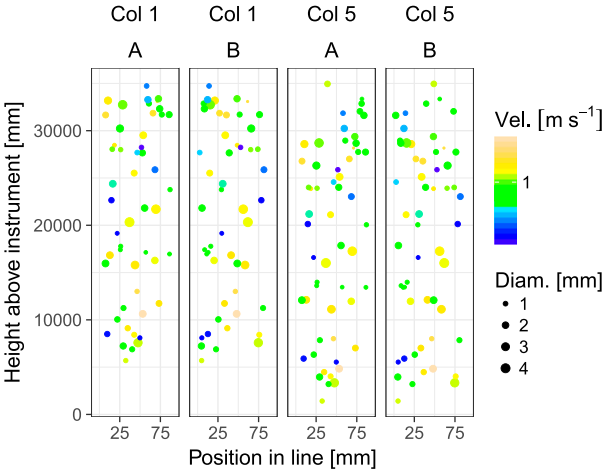

FIG. 3. Examples of two of the reconstructed columns. Col 1 and Col 5 correspond to the first and fifth second, respectively, of the studied hour of precipitation on 11 Jan 2015. A and B correspond to the two 2DVD cameras. Points show particle locations in the column, point size shows recorded particle (maximum) width, and color shows velocity. Diameters calculated using method of Huang et al. (2010).

uniformly in the vertical and performed the same multifractal analysis on these homogeneously distributed fields. Figure 4 shows the difference between the reconstructed columns and the homogeneously distributed ones. Before analyses were performed, all values were normalized by the mean of all data across all realizations.

c. *Time series*

Because the 2DVD provides information about individual particles, we could construct time series at a chosen time resolution. We used the following formula to estimate precipitation intensity:

$$\tilde{R}_p = \sum_n^{N_P} \left(\frac{10^3\, m_n}{S_n \Delta t} \right)^p, \tag{16}$$

where S_n (mm^2) is the sampling area, Δt (h) is the temporal resolution, N_P is the total number of particles over which the sum is taken (i.e., the number of particles that fell through the collection area during Δt), and we assume that 1 g represents exactly $1000\,\mathrm{mm}^3$ of water. The sampling area S_n is calculated for each particle's width from camera A [W_A (mm)] and width from camera B [W_B (mm)] as $S_n = (88 - W_A/2)(88 - W_B/2)$, because particles that were not fully inside the selected sampling area were removed, thus reducing the effective sampling area (e.g., Schönhuber et al. 2008; Battaglia et al. 2010). Parameter p is again a power, such that when $p = 0$, the quantity produced is the number of particles observed per time step, and when $p = 1$ the intensity is given in millimeters per hour so that it is equivalent to rain rate if the precipitation was liquid.

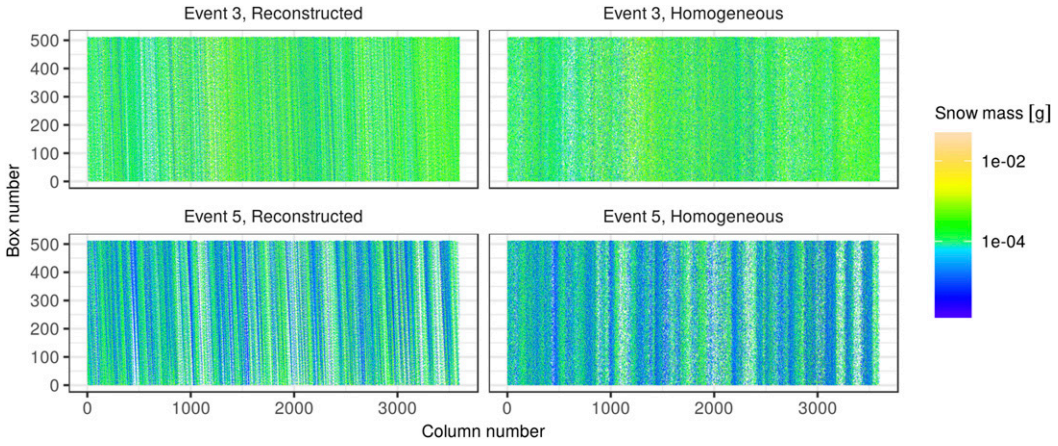

FIG. 4. Snow mass per box and per column, for events 3 and 5, showing the difference between reconstructed and homogeneously distributed particles. In the reconstructed fields, the particles falling toward the 2DVD over time are visible as oblique patterns. In the analyzed fields, zeros were filled in where no mass was recorded.

For each event, we calculated a time series for a temporal resolution of 0.1 s and cut the time series so that it contained a power-of-two number of time steps. The subset chosen contained the largest number of recorded particles. Figure 5 shows examples of time series, with the analyzed portions shown in red. Individual data points were normalized by the overall ensemble mean before analyses were made. For comparison with the recorded time series, homogeneous time series were created by randomly sampling without replacement from the measured time series values to randomize their order.

d. Particle accumulations

Particle accumulation maps were calculated using particle positions and widths in millimeters from each camera, projected onto a grid of pixels with a pixel side length of 0.1 mm. The sampling area was cropped so that it had a power-of-two number of pixels per side; the resulting maps are at a resolution of 512 × 512 pixels. The area in the center of the sampled area was used to reduce any potential edge effects. Accumulation maps were calculated by number of accumulated particles per map, for 10, 50, and 100 particles, up to a maximum of 200 maps, each separate in time. For each map, each pixel contained the number of snowflakes that covered that pixel when they were measured. Figure 6 shows examples of particle maps. The rectangular shapes of the particles are because the particle is assumed to completely cover the area defined by the widths from each camera. These maps were considered to contain realizations of a two-dimensional field. The numbers of maps of snowflake accumulations calculated for each

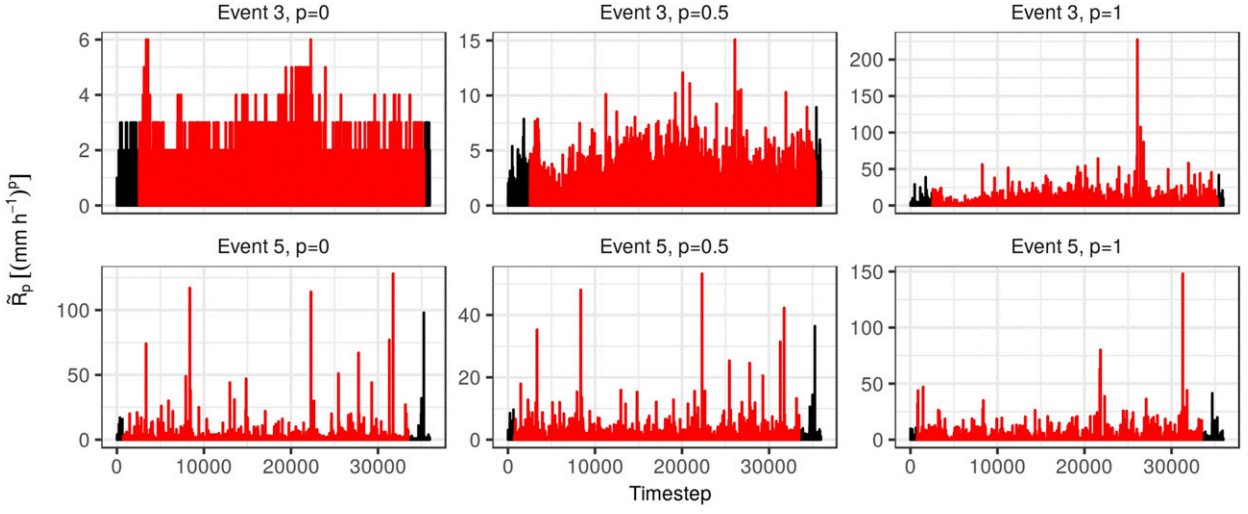

FIG. 5. Time series at 100-ms resolution, showing estimated solid precipitation liquid water intensity $\tilde{R}_p$ [(mm h^{-1})^p] for events 3 and 5, by power p. The analyzed sections are shown in red.

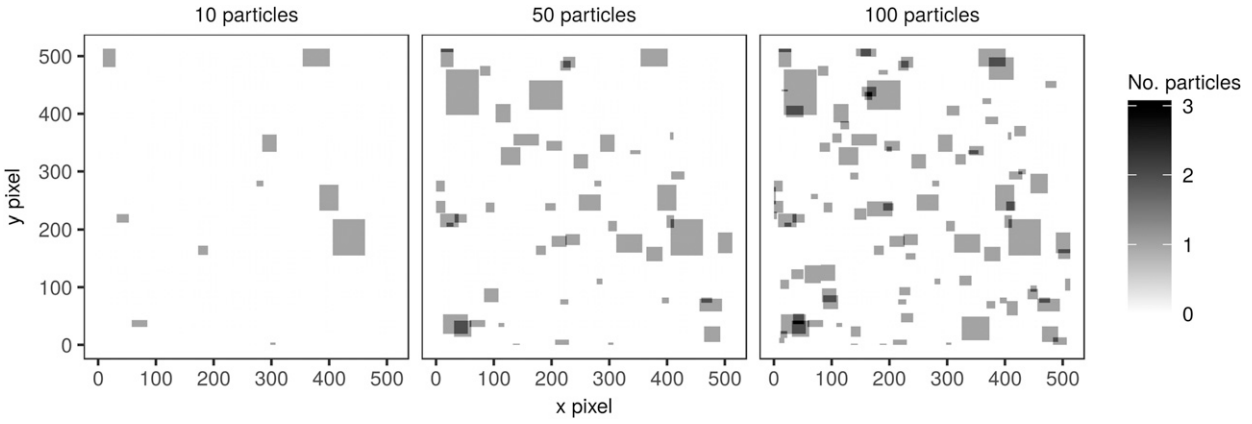

FIG. 6. Examples of accumulation maps from the 11 Jan 2015 event, showing the first maps containing 10, 50, and 100 particles respectively.

event are shown in Table 2. Just as with the other "cuts" we used, these data were processed in sets (by number of accumulated particles) and for each set the data were normalized by the ensemble mean of the set data.

e. *Multifractal analysis*

For each type of data analyzed (vertical columns, time series, and accumulation maps), we performed multifractal analysis. For the vertical columns and time series, analysis was performed for values of p of 0 (particle concentration), 0.5, and 1 (particle mass). For the accumulation maps, analyses were performed for 10, 50, and 100 particles per map. First, spectral analysis and TM analysis were used together to identify scaling regimes; the scaling regimes were manually identified, with the criteria being to 1) observe scaling in the spectral analysis (the mean of the field, represented by resolution at $k = 1$, was ignored) and 2) ensure that the TM correlation coefficient r^2 was maximized. DTM analysis was performed for $q = 1.5$. Spectral analysis was used to determine whether any additional fractional integration was required before TM and DTM were used. As a first guess of H for the fractional integration, we used $\tilde{H} = (\beta - 1)/2$. If $\tilde{H}$ was less than zero, fractional integration of order $\tilde{H}$ was used on each realization before TM and DTM analyses were applied. Informed by the identified scaling regimes, DTM analysis was used to estimate values of α, C_1, γ_s, q_s, and H. To calculate α and C_1, the slope of the DTM line on a neighborhood of seven points on the $\log_{10}(\eta)$ axis was used. This axis comprises a sequence of 34 evenly spaced values of $\log_{10}(\eta)$ between -2 and 1. Fractional integration smoothed the slopes. It can be difficult to determine on which part of the line the slope should be taken. In this work, we fitted lines using the neighborhood around center points with $\log_{10}(\eta)$ values between 0 and 0.6 in steps of 0.1, selected the fit with nonzero α and the highest squared correlation coefficient, and confirmed the results via visual inspection of the DTM curves.

5. Results

In this section we show results and interpretations of UM analysis of the three spatiotemporal "cuts" in turn.

a. *Vertical columns*

Exactly the same analyses were performed on both reconstructed vertical columns and on the columns in which the particles were distributed randomly. This was to ensure that potential scaling results found on the reconstructed columns were not artifacts of the analysis methods. The first step in all our multifractal analyses is to

TABLE 2. The number of maps found per number of within-map particles, per event. The snapshots were made using particles recorded in a $51.2 \times 51.2\,\text{mm}^2$ subset of the 2DVD measurement area.

Event	Particles	No. maps
1	10	200
1	50	138
1	100	69
2	10	200
2	50	101
2	100	50
3	10	200
3	50	99
3	100	49
4	10	200
4	50	88
4	100	44
5	10	200
5	50	101
5	100	50
6	10	200
6	50	126
6	100	63

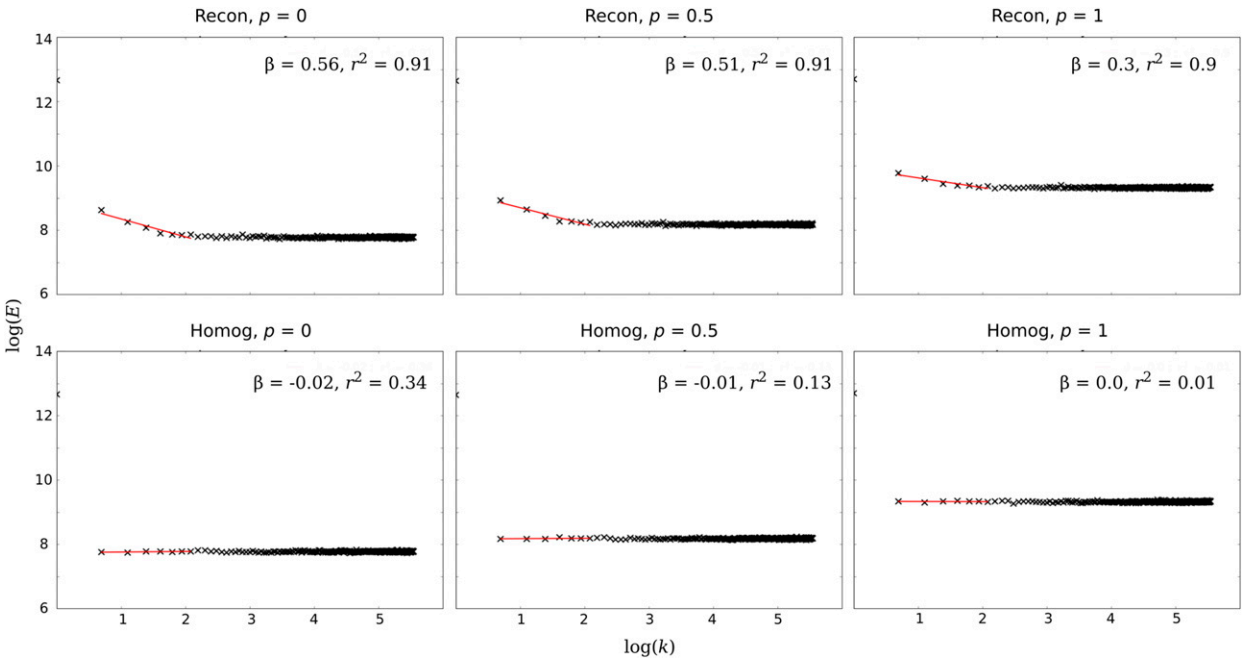

FIG. 7. Spectral analyses for vertical columns, for the analyzed hour of precipitation on 11 Jan 2015. Shown are results for $p = 0$, $p = 0.5$, and $p = 1$ for both (top) reconstructed particle positions (Recon) and (bottom) homogeneously assigned (Homog) particle positions.

look at spectral analyses of the fields to see whether scaling exists, and if so, which ranges of scales display multifractal properties. Example plots for a single hour of precipitation (event 3) are shown in Fig. 7. Here we compare the spectral analysis of reconstructed vertical column data and of vertical columns in which the particles were randomly distributed in a uniform way.

The spectral analysis of fields with homogeneous particle distributions shows, as expected, a slope of zero. On the other hand, the reconstructed columns show a section in which scaling is observed over scales down to about 4 m in all cases, and down to 1–2 m on the events with light wind and $p = 0$. Just over half of these fields had negative values of $\tilde{H}$, and thus on those fields, fractional integration of order $\tilde{H}$ was performed before conducting the TM and DTM analyses. TM and DTM analyses were carried out for resolutions of 1–8, corresponding to observational scales of 35–4.38 m. The scaling regimes shown in the TM analyses often extended more toward the small scale, as can be seen in Fig. 8, in which the scaling regime seems to extend to about $\lambda = 64$ or about 0.5 m. For consistency across the spectral analysis results, however, we analyzed the same scales for all fields. Results for the analyses of vertical columns are shown in Table 3. TM and DTM analysis plots for the vertical columns in the example hour are shown in Fig. 8.

The spectral analyses for vertical columns show scaling for particle concentrations ($p = 0$) for scales

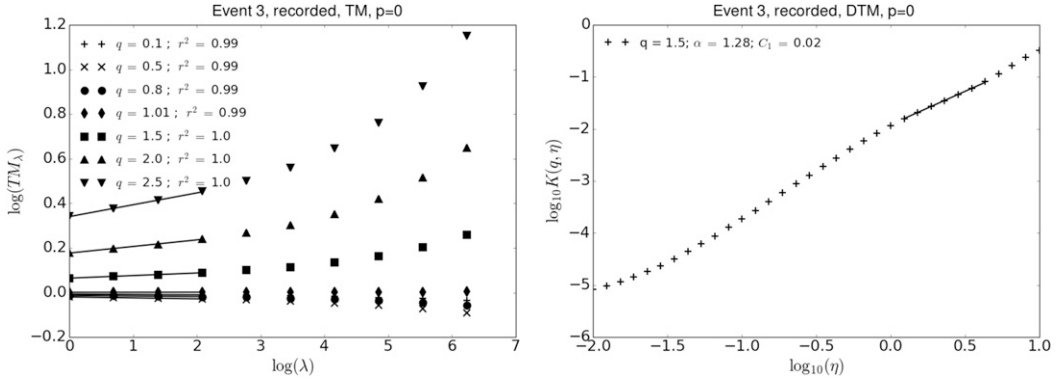

FIG. 8. TM and DTM analyses for vertical columns in the analyzed hour of precipitation on 11 Jan 2015, for $p = 0$. In this plot, $\mathrm{TM}_\lambda = \langle \varepsilon_\lambda^q \rangle$ for a given moment order q, and η is the power to which the field is raised then upscaled.

TABLE 3. Multifractal analysis results for the reconstructed vertical columns, by event E, for scales from 35 m to 4.38 m (β calculated for 17.5 m to 4.38 m). r^2 (spec) is squared correlation coefficient for the spectral slope, and r^2 (TM) is the squared correlation coefficient for the TM analysis over the selected scales. The correlation scores for the TM analyses are higher after the use of fractional integration, which introduces correlation.

Event	p	β	r^2 (spec)	r^2 (TM)	α	C_1	γ_s	q_s	H
1	0.0	0.33	0.95	0.99	1.47	0.02	0.15	17.18	−0.32
1	0.5	0.27	0.92	0.99	1.57	0.02	0.18	13.09	−0.35
1	1.0	0.14	0.69	0.99	1.87	0.02	0.25	7.75	−0.41
2	0.0	1.23	0.90	1.00	1.99	0.01	0.20	9.30	0.13
2	0.5	1.07	0.91	1.00	2.09	0.02	0.28	6.32	0.06
2	1.0	0.49	0.86	1.00	2.21	0.02	0.31	5.55	−0.23
3	0.0	0.56	0.91	1.00	1.28	0.02	0.14	22.48	−0.21
3	0.5	0.51	0.91	0.99	1.65	0.02	0.20	10.78	−0.23
3	1.0	0.30	0.90	0.99	2.07	0.02	0.28	6.41	−0.33
4	0.0	1.45	0.99	1.00	1.94	0.08	0.49	3.57	0.31
4	0.5	1.40	0.97	1.00	1.88	0.06	0.41	4.40	0.26
4	1.0	0.95	0.96	1.00	2.88	0.06	0.54	2.70	0.06
5	0.0	1.27	0.99	1.00	1.98	0.08	0.49	3.52	0.22
5	0.5	1.09	0.97	1.00	2.06	0.04	0.38	4.66	0.09
5	1.0	0.74	0.94	1.00	2.98	0.02	0.42	3.47	−0.10
6	0.0	1.46	1.00	1.00	1.82	0.12	0.55	3.15	0.34
6	0.5	1.38	0.98	1.00	2.07	0.07	0.47	3.64	0.26
6	1.0	0.78	0.93	1.00	2.83	0.03	0.43	3.49	−0.07

down to about 4 m. As the power p increases, however, the quality of the scaling, as measured by β and its associated correlation coefficient, tends to reduce. This is visible in Fig. 7 and is likely because increased power implies a larger impact of heavier snowflakes. Heavier flakes are rarer and therefore show less scaling over the 35-m column that we studied. We hypothesize that larger (and thus heavier) snowflakes decorrelate from atmospheric turbulence at larger scales, but the studied scales were not large enough to confirm this. We focus on the case where good scaling was observed, that is, $p = 0$ corresponding to columns containing the vertical distribution of particle concentrations.

TM and DTM analysis were also performed for the homogeneously distributed particle fields, after fractional integration using the values of β for the reconstructed fields (when those fields had integration performed). These results are shown in Table 4. They show that with homogeneously distributed particle

TABLE 4. Multifractal analysis results for vertical columns with homogeneous particle positions, fractionally integrated (when appropriate) using values of β in Table 3. Results are shown by event E, for scales from 35 m to 4.38 m (β calculated for 17.5 m to 4.38 m). r^2 (spec) and r^2 (TM) defined as for Table 3.

Event	p	β	r^2 (spec)	r^2 (TM)	α	C_1	γ_s	q_s	H
1	0.0	0.01	0.14	0.98	1.48	0.01	0.12	21.32	−0.33
1	0.5	0.02	0.43	0.98	1.60	0.01	0.15	15.36	−0.35
1	1.0	0.03	0.56	0.99	1.90	0.02	0.23	8.42	−0.41
2	0.0	0.03	0.32	0.92	2.60	0.00	0.15	10.41	0.12
2	0.5	0.00	0.01	0.92	2.79	0.01	0.25	6.05	0.04
2	1.0	−0.02	0.23	0.97	3.10	0.01	0.31	4.76	−0.24
3	0.0	−0.02	0.34	0.96	1.28	0.01	0.10	33.97	−0.21
3	0.5	−0.01	0.13	0.96	1.75	0.01	0.17	12.73	−0.23
3	1.0	0.00	0.01	0.98	2.14	0.01	0.25	7.20	−0.33
4	0.0	0.03	0.70	0.92	2.34	0.00	0.13	13.77	0.23
4	0.5	−0.01	0.12	0.93	2.58	0.01	0.25	6.53	0.21
4	1.0	−0.05	0.50	0.94	3.59	0.02	0.45	3.06	0.01
5	0.0	−0.01	0.06	0.93	2.47	0.00	0.14	12.26	0.14
5	0.5	−0.01	0.01	0.93	2.53	0.01	0.26	6.23	0.06
5	1.0	−0.00	0.00	0.96	3.47	0.01	0.34	4.05	−0.12
6	0.0	−0.01	0.25	0.92	2.36	0.00	0.10	16.57	0.23
6	0.5	0.01	0.17	0.92	2.64	0.01	0.23	6.84	0.20
6	1.0	0.02	0.20	0.94	3.53	0.01	0.35	3.93	−0.09

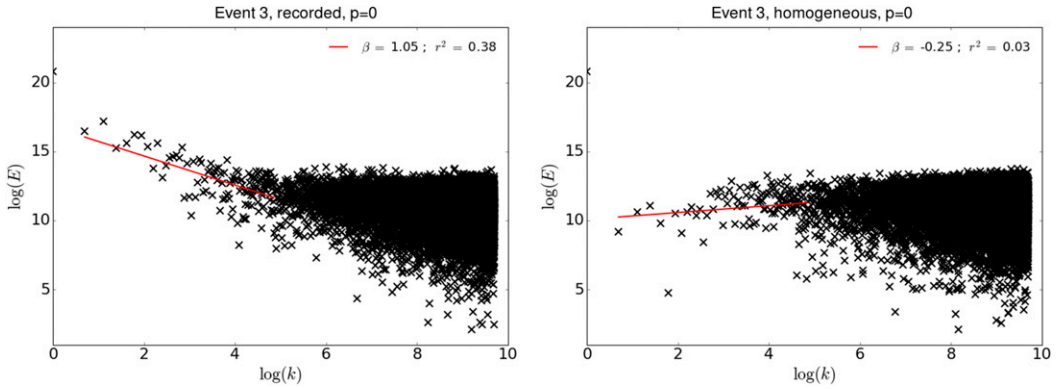

FIG. 9. Spectral analyses for the analyzed time series of precipitation on 11 Jan 2015, for recorded and homogeneous time series.

positions, β was close to zero. Where less or no scaling is observed, for example, for event 1 with $p = 1$, the results are similar between the two sets, indicating that the reconstructed columns contained no clustering and little scaling, and that in those cases the results of the TM and DTM analyses are rather an artifact of the fractional integration that was applied. When scaling is evident, however, there are differences shown between the homogeneous and reconstructed results, which shows that the obtained values are representative of the underlying physical process and not an artifact of the analysis technique. For example, when $p = 0$, there are, in most cases, differences in the results for the homogeneous and reconstructed fields. The differences are particularly clear for the maximum singularity and moment order in these cases. We note again that in the light wind cases the assumptions involved in reconstructing the vertical column have a weaker basis. In general, the differences in q_s tend to decrease with increasing value of the power p, which aligns with the results of the spectral analyses. The TM and DTM analyses show values of α that are outside normal limits (i.e., greater than 2). We hypothesize that these high values are due to estimation uncertainty in the DTM analyses, as well as in the determination of the spectral slope and thus the degree of fractional integration applied. They demonstrate the difficulty of estimating exact values for multifractal properties on this dataset. Given these uncertainties, the strongest evidence for scaling in the vertical columns comes from the spectral analyses, in which there is a clear difference between the measured and uniformly distributed fields.

In all cases, analyses were carried out on scales ranging from 35 to 4.38 m, meaning that the results are valid only on this range. Further investigations would be needed to extend these results to larger scales. For these analyzed scales and $p = 0$, the DTM analysis shows a fractal codimension C_1 of up to ~0.12, indicating that the mean field exhibits a low mean intermittency. In other words, the fractal codimension of the portion of the field that is greater than the mean singularity (for $q = 1$) is small. The multifractality index α is high, which means that this codimension changes rapidly as it is thresholded at higher singularities. The differences between reconstructed and homogeneously distributed particle concentrations offers evidence that scaling is, at times, present in vertical snowflake concentrations for scales between 35 and about 4.4 m, and sometimes down to 0.5 m. This evidence of scaling opens the possibility of numerical simulations of vertical snowfall fields on this range of scales, using UM. However, noise in the data, the small dataset, and associated estimation errors mean that complete simulations would require further investigation to precisely determine UM parameters.

b. *Time series*

An example of spectral analysis results for the time series is shown in Fig. 9. The spectral analyses results were noisy and had low correlation coefficients for spectral slope, indicating that the quality of the scaling is limited. This is common behavior when only one field realization is available, as was the case for each time series. It was not possible to distinguish different scaling regimes from these analyses alone, although they suggested that scaling may be found in some events on scales from about 1 h to about 1 min. For scales under 1 min, the spectral analysis results were inconclusive. Spectral analysis was run for scales from ~27 min to 25.6 s. The values of β produced by spectral analysis of the time series data showed a small spectral slope and therefore some scaling for most events, which was confirmed by comparisons with time series in which the data order was randomized. In these randomized cases, little or no scaling was observed. The events with light

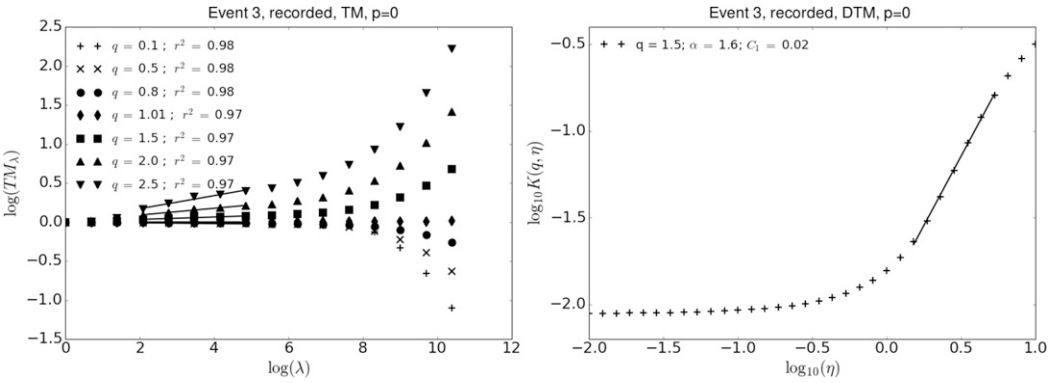

FIG. 10. TM and DTM analyses for the analyzed time series of precipitation on 11 Jan 2015.

wind showed considerably weaker scaling than the events in calm conditions, with very little scaling shown in the spectral analysis results for events 4 and 6. The values of $\tilde{H}$ returned by the spectral analyses were usually negative, so in these cases a fractional integration of order $\tilde{H}$ was performed on each time series. TM analyses on the resulting fields further confirm that scaling exists in most of the analyzed events between scales of ~7 min and 25.6 s, often with the scaling break at ~7 min. In some cases the TM plots suggest that scaling exists down to scales of about half a second, but the spectral analyses are very noisy for these events and scales. Examples of TM and DTM plots for the time series analysis are shown in Fig. 10. UM analysis results for the time series are shown in Table 5.

Just as for the vertical columns, we compared the results to those using exactly the same fractional integration and processing on randomized fields. In the case of the time series, the UM results were different for every event and value of p, so we consider that the scaling shown by these results is not introduced by the data processing. While the low amount of data means that we should not put too much emphasis on individual results, and while some outlier values of α were estimated, we conclude that scaling can exist in the time series of snowfall over scales from ~7 min down to 25.6 s. We note that at the average particle fall velocity (1.1 m s^{-1}), the lower limit of the scaling regime observed in vertical columns (4.4 m) equates to a time series scale of about 4 s. While the TM analyses showed scaling at higher resolutions, given the available data and the poor quality of the time series scaling results on this range of scales, we are not able to state definitively whether scaling exists in the time series for scaling regimes from ~25 to 4 s.

TABLE 5. UM analysis results for recorded snowfall time series, for scales from ~7 min to 25.6 s (β calculated for scales from 27 min to 25.6 s). Parameters r^2 (spec) and r^2 (TM) defined as for Table 3.

Event	p	β	r^2 (spec)	r^2 (TM)	α	C_1	γ_s	q_s	H
1	0.0	0.70	0.14	0.97	1.53	0.00	0.06	41.44	−0.15
1	0.5	0.52	0.10	0.98	1.52	0.00	0.05	53.22	−0.24
1	1.0	0.51	0.11	0.96	1.83	0.00	0.09	23.68	−0.24
2	0.0	0.72	0.20	0.98	1.57	0.02	0.20	11.36	−0.12
2	0.5	0.67	0.23	0.99	1.99	0.01	0.22	8.73	−0.15
2	1.0	0.53	0.12	0.99	2.33	0.00	0.12	14.78	−0.23
3	0.0	1.05	0.38	0.97	1.60	0.02	0.18	13.09	0.04
3	0.5	1.00	0.34	0.96	0.82	0.03	0.10	74.00	0.02
3	1.0	0.83	0.21	0.96	2.52	0.00	0.11	15.21	−0.08
4	0.0	0.01	0.00	0.98	2.86	0.00	0.23	6.53	−0.49
4	0.5	0.15	0.02	0.98	2.90	0.01	0.26	5.83	−0.42
4	1.0	0.34	0.08	0.97	2.88	0.01	0.29	5.25	−0.32
5	0.0	0.26	0.03	1.00	2.66	0.02	0.36	4.29	−0.34
5	0.5	0.42	0.07	0.99	2.26	0.01	0.26	6.51	−0.27
5	1.0	0.37	0.06	0.96	2.32	0.00	0.17	10.09	−0.31
6	0.0	0.05	0.00	1.00	2.03	0.01	0.23	8.16	−0.46
6	0.5	0.04	0.00	0.99	2.78	0.01	0.25	6.15	−0.47
6	1.0	0.16	0.02	0.96	2.70	0.01	0.26	6.01	−0.41

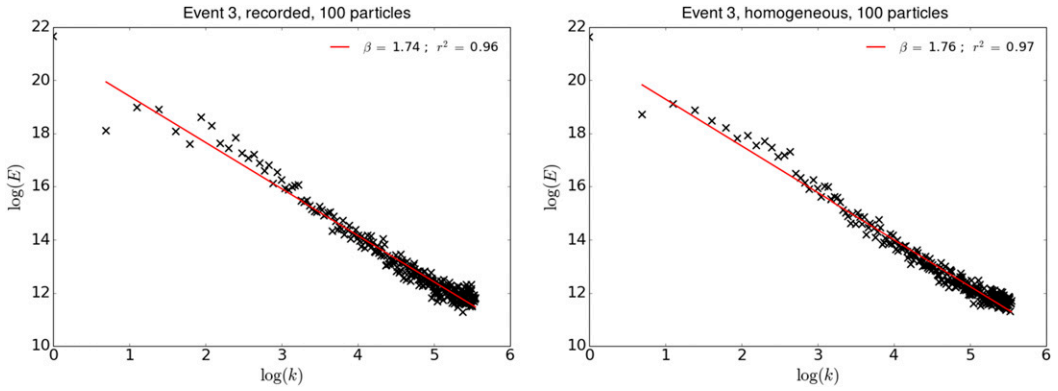

FIG. 11. Spectral analyses for the analyzed snow accumulation maps on 11 Jan 2015.

c. *Particle accumulations*

Results of spectral analysis for accumulation maps with 100 particles, for measured and randomly spatially distributed particle fields, are shown as an example in Fig. 11. The results of spectral analysis using uniformly randomly distributed particles are similar to those for the measured distributions in space, as is shown in Table 6. This is evidence that no scaling is shown in the measured distributions. For all values of p, the values of β were significantly lower than two, the dimension of the field. We conclude that at the analyzed scale of $5.12 \times 5.12\,\mathrm{cm}^2$, the snow particles exhibit the same behavior as if they were distributed homogeneously—that is, as if their positions were drawn from a uniform distribution. This conclusion agrees with the analysis of the vertical columns, which showed no scaling for particle concentrations at scales below ~0.5–4.4 m. These results also suggest that the 2DVD displays homogeneous sampling characteristics.

The exceedance probabilities of the time required to observe 10, 50, 100, and 500 snowflakes were calculated [as shown for liquid precipitation in Gires et al. (2015)]. These results are shown in Fig. 12. There is power-law behavior (a straight line in the log–log plot) shown for some temporal scales, for example, for accumulations of 50 snowflakes between time periods of about 10 and 30 s. At the mean observed snowflake velocity in our six events ($1.1\,\mathrm{m\,s}^{-1}$), this range of times corresponds to spatial scales of 11–33 m. The power-law behavior thus supports the idea that there is some scaling behavior in snow particle distributions over scales on the order of meters to tens of meters in this context, as we showed in section 5a.

6. Conclusions

In this paper we have shown the results of UM analyses of snowfall at high spatial and temporal resolutions. Methodologies similar to Gires et al. (2015) were used to analyze snowfall data. Six 1-h-long periods of snowfall, with 3 h in calm conditions and 3 h in light wind conditions, were studied. The data were collected by a 2DVD in the Swiss Alps in the northern winter of 2014/15. Multifractal analyses were performed on ballistically reconstructed vertical columns and high-resolution time series of quantities derived from particle concentration and mass, and on two-dimensional snowfall accumulation maps within the sampling window of the 2DVD.

There were some difficulties in estimation of the multifractal parameters, due to the small range of scales it was possible to investigate, and the scaling observed was generally of poor quality. With the available data, scaling was observed in the vertical columns of particle concentrations between scales of about 35 and 4.4 m (and sometimes down to 0.5 m). At smaller scales the vertical fields behaved as if they were uniformly

TABLE 6. Results of spectral analysis on accumulated particle maps, for the number of particles (Num P), for measured (meas) and homogeneously (hom) distributed particle maps, per event (E).

E	Num P	β (meas)	r^2 (meas)	β (hom)	r^2 (hom)
1	10	1.62	0.93	1.60	0.94
1	50	1.71	0.96	1.71	0.96
1	100	1.72	0.97	1.75	0.97
2	10	1.69	0.95	1.69	0.95
2	50	1.64	0.96	1.65	0.95
2	100	1.56	0.93	1.57	0.94
3	10	1.71	0.96	1.76	0.96
3	50	1.74	0.97	1.74	0.97
3	100	1.74	0.96	1.76	0.97
4	10	1.38	0.88	1.42	0.88
4	50	1.49	0.90	1.53	0.92
4	100	1.53	0.92	1.55	0.93
5	10	1.75	0.96	1.74	0.96
5	50	1.36	0.88	1.36	0.88
5	100	1.62	0.96	1.63	0.97
6	10	1.54	0.92	1.49	0.91
6	50	1.56	0.94	1.58	0.95
6	100	1.56	0.95	1.58	0.95

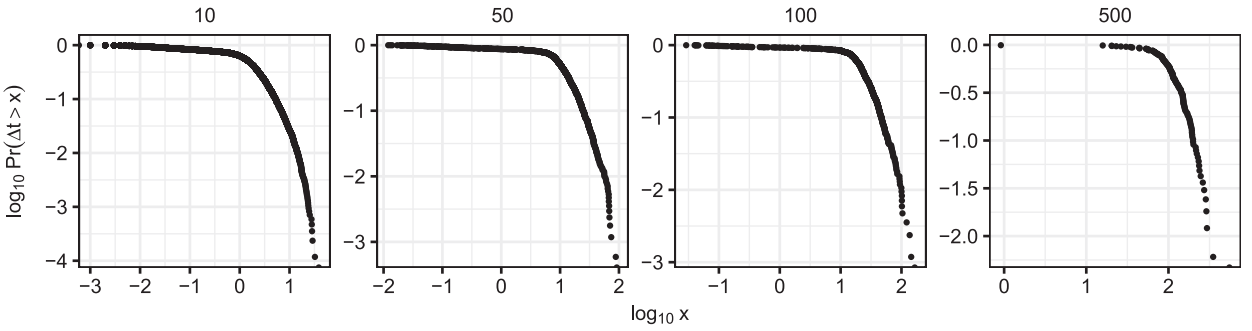

FIG. 12. Exceedance probabilities for the time t required to observe n snowflakes, where n is equal to 10, 50, 100, and 500.

distributed. The results suggested that scaling was present in some of the snowfall intensity time series, for scales from ~7 min to ~26 s; this limit of about 26 s is similar to the results of Fabry (1996). Analysis of two-dimensional snowflake accumulation maps over a subset of the small sampling window of the 2DVD showed no scaling, which agreed with the other results that showed little or no scaling at such a small scale. These results are similar to those previously shown for rainfall (Gires et al. 2015), in that scaling is found down to some lower limit in space and time. The lower limits found differ (e.g., ~4 m compared to 0.5 m in vertical space). Our results suggest that the scaling regime in vertical columns of snow could extend to a similar scale as found for rain, but more snowfall data are required to confirm that these differences between snowfall and rain are significant. Further investigations on larger datasets are needed to extend the results to a wider range of scales and to obtain more robust UM parameter estimates that could be used to fully simulate snowfall fields.

Acknowledgments. The authors thank Daniel Wolfensberger, Loïc Habegger, Jacopo Grazioli, Christophe Praz, and Marc Ruesch for helping set up and maintain the 2DVD. We thank the WSL Institute for Snow and Avalanche Research SLF, and the Office Fédéral de Météorologie et de Climatologie MétéoSuisse, for hosting the 2DVD at the Versuchsfeld site. The meteorological data (temperature, wind speed, and laser disdrometer solid precipitation intensity) were obtained from the Solid Precipitation Intercomparison Experiment (SPICE) and MétéoSuisse. SPICE disclaimer: results presented in this work were obtained as part of the Solid Precipitation InterComparison Experiment (SPICE), conducted on behalf of the World Meteorological Organization (WMO) Commission for Instruments and Methods of Observation (CIMO). The analysis and views described herein are those of the author(s) at this time, and do not necessarily represent the official outcome of WMO SPICE. Mention of commercial companies or products is solely for the purposes of information and assessment within the scope of the present work, and does not constitute an endorsement by the author(s) or WMO. This study was supported by the Swiss National Science Foundation under Grant 2000021_140669. The authors thank the Partenariat Hubert Curien–Germaine de Staël (Project 32709UK) for financial support that made this collaboration possible. The authors from École des Ponts ParisTech gratefully acknowledge partial financial support from the chair "Hydrology for Resilient Cities" (endowed by Veolia) of École des Ponts ParisTech. We thank two anonymous reviewers for their constructive reviews.

REFERENCES

Battaglia, A., E. Rustemeier, A. Tokay, U. Blahak, and C. Simmer, 2010: PARSIVEL snow observations: A critical assessment. *J. Atmos. Oceanic Technol.*, **27**, 333–344, doi:10.1175/2009JTECHA1332.1.

Böhm, H. P., 1989: A general equation for the terminal fall speed of solid hydrometeors. *J. Atmos. Sci.*, **46**, 2419–2427, doi:10.1175/1520-0469(1989)046<2419:AGEFTT>2.0.CO;2.

Deems, J. S., S. R. Fassnacht, and K. J. Elder, 2006: Fractal distribution of snow depth from lidar data. *J. Hydrometeor.*, **7**, 285–297, doi:10.1175/JHM487.1.

De Lima, M., and J. Grasman, 1999: Multifractal analysis of 15-min and daily rainfall from a semi-arid region in Portugal. *J. Hydrol.*, **220**, 1–11, doi:10.1016/S0022-1694(99)00053-0.

——, and J. De Lima, 2009: Investigating the multifractality of point precipitation in the Madeira archipelago. *Nonlinear Processes Geophys.*, **16**, 299–311, doi:10.5194/npg-16-299-2009.

De Montera, L., L. Barthès, C. Mallet, and P. Golé, 2009: The effect of rain-no rain intermittency on the estimation of the universal multifractals model parameters. *J. Hydrometeor.*, **10**, 493–506, doi:10.1175/2008JHM1040.1.

Fabry, F., 1996: On the determination of scale ranges for precipitation fields. *J. Geophys. Res.*, **101**, 12 819–12 826, doi:10.1029/96JD00718.

Fraedrich, K., and C. Larnder, 1993: Scaling regimes of composite rainfall time series. *Tellus*, **45A**, 289–298, doi:10.3402/tellusa.v45i4.14893.

Gires, A., I. Tchiguirinskaia, D. Schertzer, and S. Lovejoy, 2011: Analyses multifractales et spatio-temporelles des précipitations du modèle Méso-NH et des données radar. *Hydrol. Sci. J.*, **56**, 380–396, doi:10.1080/02626667.2011.564174.

——, ——, ——, A. Schellart, A. Berne, and S. Lovejoy, 2014: Influence of small scale rainfall variability on standard comparison tools between radar and rain gauge data. *Atmos. Res.*, **138**, 125–138, doi:10.1016/j.atmosres.2013.11.008.

——, ——, ——, and A. Berne, 2015: 2DVD data revisited: Multifractal insights into cuts of the spatiotemporal rainfall process. *J. Hydrometeor.*, **16**, 548–562, doi:10.1175/JHM-D-14-0127.1.

——, ——, and ——, 2016: Multifractal comparison of the outputs of two optical disdrometers. *Hydrol. Sci. J.*, **61**, 1641–1651, doi:10.1080/02626667.2015.1055270.

Goodison, B., P. Louie, and D. Yang, 1998: WMO solid precipitation intercomparison. Instruments and Observing Methods Rep. 67, WMO/TD-872, 212 pp. [Available online at https://www.wmo.int/pages/prog/www/IMOP/publications/IOM-67-solid-precip/WMOtd872.pdf.]

Granger, R. J., J. W. Pomeroy, and J. Parviainen, 2002: Boundary-layer integration approach to advection of sensible heat to a patchy snow cover. *Hydrol. Processes*, **16**, 3559–3569, doi:10.1002/hyp.1227.

Hanesch, M., 1999: Fall velocity and shape of snowflakes. Ph.D. thesis, Swiss Federal Institute of Technology Zurich, 117 pp.

Huang, G.-J., V. N. Bringi, R. Cifelli, D. Hudak, and W. A. Petersen, 2010: A methodology to derive radar reflectivity–liquid equivalent snow rate relations using C-band radar and a 2D video disdrometer. *J. Atmos. Oceanic Technol.*, **27**, 637–651, doi:10.1175/2009JTECHA1284.1.

——, ——, D. Moisseev, W. Petersen, L. Bliven, and D. Hudak, 2015: Use of 2D-video disdrometer to derive mean density–size and Z_e–SR relations: Four snow cases from the light precipitation validation experiment. *Atmos. Res.*, **153**, 34–48, doi:10.1016/j.atmosres.2014.07.013.

Hubert, P., and Coauthors, 1993: Multifractals and extreme rainfall events. *Geophys. Res. Lett.*, **20**, 931–934, doi:10.1029/93GL01245.

Iggy Litaor, M., T. Seastedt, and D. Walker, 2002: Spatial analysis of selected soil attributes across an alpine topographic/snow gradient. *Landscape Ecol.*, **17**, 71–85, doi:10.1023/A:1015216400909.

Kruger, A., and W. F. Krajewski, 2002: Two-dimensional video disdrometer: A description. *J. Atmos. Oceanic Technol.*, **19**, 602–617, doi:10.1175/1520-0426(2002)019<0602:TDVDAD>2.0.CO;2.

Lavallée, D., S. Lovejoy, D. Schertzer, and P. Ladoy, 1993: Nonlinear variability and landscape topography: Multifractal analysis and simulation. *Fractals in Geography*, L. de Cola and N. Lam, Eds., Prentice-Hall, 158–192.

Löffler-Mang, M., and J. Joss, 2000: An optical disdrometer for measuring size and velocity of hydrometeors. *J. Atmos. Oceanic Technol.*, **17**, 130–139, doi:10.1175/1520-0426(2000)017<0130:AODFMS>2.0.CO;2.

Lovejoy, S., and D. Schertzer, 1995: Multifractals and rain. *New Uncertainty Concepts in Hydrology and Water Resources*, Z. W. Kundzewicz, Ed., Cambridge University Press, 61–103.

——, ——, and A. Tsonis, 1987: Functional box-counting and multiple elliptical dimensions in rain. *Science*, **235**, 1036–1038, doi:10.1126/science.235.4792.1036.

——, ——, and V. Allaire, 2008: The remarkable wide range spatial scaling of TRMM precipitation. *Atmos. Res.*, **90**, 10–32, doi:10.1016/j.atmosres.2008.02.016.

Mandapaka, P. V., P. Lewandowski, W. Eichinger, and W. F. Krajewski, 2009: Multiscaling analysis of high resolution space-time lidar-rainfall. *Nonlinear Processes Geophys.*, **16**, 579–586, doi:10.5194/npg-16-579-2009.

Molnar, P., and P. Burlando, 2008: Variability in the scale properties of high-resolution precipitation data in the alpine climate of Switzerland. *Water Resour. Res.*, **44**, W10404, doi:10.1029/2007WR006142.

Nykanen, D. K., and D. Harris, 2003: Orographic influences on the multiscale statistical properties of precipitation. *J. Geophys. Res.*, **108**, 8381, doi:10.1029/2001JD001518.

Olsson, J., 1995: Limits and characteristics of the multifractal behaviour of a high-resolution rainfall time series. *Nonlinear Processes Geophys.*, **2**, 23–29, doi:10.5194/npg-2-23-1995.

Parisi, G., and U. Frish, 1985: A multifractal model of intermittency. *Turbulence and Predictability in Geophysical Fluid Dynamics*, M. R. Ghill, R. Benzi, and G. Parisi, Eds., North Holland, 111–114.

Roulet, Y.-A., A. Reverdin, and F. van den Heuvel, 2014: Commissioning report of site of Weissfluhjoch. MeteoSwiss Rep., 115 pp. [Available online at http://www.wmo.int/pages/prog/www/IMOP/intercomparisons/SPICE/Commissioning/Weissfluhjoch_V2.pdf.]

Royer, J.-F., A. Biaou, F. Chauvin, D. Schertzer, and S. Lovejoy, 2008: Multifractal analysis of the evolution of simulated precipitation over France in a climate scenario. *C. R. Geosci.*, **340**, 431–440, doi:10.1016/j.crte.2008.05.002.

Schertzer, D., and S. Lovejoy, 1987a: Physical modeling and analysis of rain and clouds by anisotropic scaling multiplicative processes. *J. Geophys. Res.*, **92**, 9693–9714, doi:10.1029/JD092iD08p09693.

——, and ——, 1987b: Singularités anisotropes, divergences des moments en turbulence: Invariance déchelle généralisée et processus multiplicatifs. *Ann. Sci. Math. Que.*, **11** (1), 139–181.

——, and ——, 1991: Nonlinear geodynamical variability: Multiple singularities, universality and observables. *Non-Linear Variability in Geophysics*, Springer, 41–82.

——, and ——, 1997: Universal multifractals do exist!: Comments on "A statistical analysis of mesoscale rainfall as a random cascade." *J. Appl. Meteor.*, **36**, 1296–1303, doi:10.1175/1520-0450(1997)036<1296:UMDECO>2.0.CO;2.

——, and ——, 2011: Multifractals, generalized scale invariance and complexity in geophysics. *Int. J. Bifurcat. Chaos*, **21**, 3417–3456, doi:10.1142/S0218127411030647.

——, I. Tchiguirinskaia, S. Lovejoy, and P. Hubert, 2010: No monsters, no miracles: In nonlinear sciences hydrology is not an outlier! *Hydrol. Sci. J.*, **55**, 965–979, doi:10.1080/02626667.2010.505173.

Schönhuber, M., G. Lammer, and W. Randeu, 2007: One decade of imaging precipitation measurement by 2D-video-distrometer. *Adv. Geosci.*, **10**, 85–90, doi:10.5194/adgeo-10-85-2007.

——, ——, and ——, 2008: The 2D-video-distrometer. *Precipitation: Advances in Measurement, Estimation and Prediction*, Springer, 3–31, doi:10.1007/978-3-540-77655-0_1.

Shook, K., and D. M. Gray, 1996: Small-scale spatial structure of shallow snowcovers. *Hydrol. Processes*, **10**, 1283–1292, doi:10.1002/(SICI)1099-1085(199610)10:10<1283::AID-HYP460>3.0.CO;2-M.

——, and ——, 1997: Synthesizing shallow seasonal snow covers. *Water Resour. Res.*, **33**, 419–426, doi:10.1029/96WR03532.

——, and J. Pomeroy, 2010: Hydrological effects of the temporal variability of the multiscaling of snowfall on the Canadian prairies. *Hydrol. Earth Syst. Sci.*, **14**, 1195–1203, doi:10.5194/hess-14-1195-2010.

Szyrmer, W., and I. Zawadzki, 2010: Snow studies. Part II: Average relationship between mass of snowflakes and their terminal fall velocity. *J. Atmos. Sci.*, **67**, 3319–3335, doi:10.1175/2010JAS3390.1.

Tessier, Y., S. Lovejoy, and D. Schertzer, 1993: Universal multifractals: Theory and observations for rain and clouds. *J. Appl. Meteor.*, **32**, 223–250, doi:10.1175/1520-0450(1993)032<0223:UMTAOF>2.0.CO;2.

——, ——, P. Hubert, D. Schertzer, and S. Pecknold, 1996: Multifractal analysis and modeling of rainfall and river flows and scaling, causal transfer functions. *J. Geophys. Res.*, **101**, 26 427–26 440, doi:10.1029/96JD01799.

Tokay, A., W. A. Petersen, P. Gatlin, and M. Wingo, 2013: Comparison of raindrop size distribution measurements by collocated disdrometers. *J. Atmos. Oceanic Technol.*, **30**, 1672–1690, doi:10.1175/JTECH-D-12-00163.1.

Verrier, S., L. De Montera, L. Barthès, and C. Mallet, 2010: Multifractal analysis of African monsoon rain fields, taking into account the zero rain-rate problem. *J. Hydrol.*, **389**, 111–120, doi:10.1016/j.jhydrol.2010.05.035.

Yang, D., 2014: Double fence intercomparison reference (DFIR) vs. bush gauge for true snowfall measurement. *J. Hydrol.*, **509**, 94–100, doi:10.1016/j.jhydrol.2013.08.052.